energies

MDPI

Article

Impact of Vertical Receiver Coil Count on Energy Transfer Efficiency in Dynamic Wireless Electric Vehicle Charging

Itay Garrofy [1], Yasha Nikulshin [1,2] and Shuki Wolfus [1,*]

[1] Department of Physics, Bar-Ilan University, Ramat-Gan 5290002, Israel; garofyi@biu.ac.il (I.G.); yasha@nt-tao.com (Y.N.)
[2] N.T. TAO Ltd., Hanagar 3, Hod Hasharon 4501306, Israel
[*] Correspondence: wolfuss@biu.ac.il

Abstract

This paper investigates how the number of receiving coils in the Vertical Coil (VC) configuration affects energy transfer efficiency in Dynamic Wireless Power Transfer (DWPT) systems for electric vehicles (EVs). Building on our previous work, in which the VC design outperformed horizontally oriented DDQ coils, receiver arrays of three to seven coils were compared using a coupled finite element and circuit co-simulation at 85 kHz across a 30 cm air gap over a 3 m pass. The relationship between coil count and harvested energy proves to be non-monotonic. Increasing the count from three to five raises the peak efficiency from approximately 85% to above 90%, and extends the high-efficiency region from roughly $|x| \lesssim 0.9$ m to the full width of the pass through the appearance of secondary peaks. Beyond five coils the spacing between neighbouring receivers narrows, mutual inductance grows, the resonant branches detune, and the harvested energy per pass falls for both the six- and seven-coil arrays. The five-coil configuration therefore maximizes the energy harvested per pass for this geometry, and the work provides simulation-based design guidelines for the VC architecture.

Keywords: dynamic wireless power transfer; vertical coil configuration; coil array optimization; mutual inductance; electric vehicle charging; energy transfer efficiency

1. Introduction

Wireless power transfer (WPT) delivers power without physical connectors, an idea that dates back to Nikola Tesla's early experiments and is now applied in systems from cell phone chargers to implantable devices [1]. For electric vehicles (EVs), Dynamic Wireless Power Transfer (DWPT) allows continuous in-motion charging [2], which reduces the need for large onboard batteries and eases range anxiety. The main obstacle is maintaining high power transfer efficiency as the vehicle moves across the transmitter coils. Coil geometry and mutual inductance strongly affect system performance [3]. Studies show that coupling coefficients, coil alignment [4], and the overall design geometry directly affect efficiency in DWPT systems [5]. Recent designs modify the coil topology to improve misalignment tolerance and spatial coverage [6]. Coil arrays are also used beyond EV charging: in free-moving wireless power applications, a multi-coil transmitter array with a star-shaped geometry delivers power to a rotating or misaligned receiver, even one oriented perpendicular to the transmitter plane [7]. Vertically oriented receivers, for example, show that coil orientation affects the coupling dynamics and efficiency [8]. In prior work, the Vertical Coil (VC) configuration, in which multiple coils are wound vertically around a

Academic Editors: Xiaofei Li and Heshou Wang

Received: 5 July 2026
Revised: 28 July 2026
Accepted: 13 August 2026
Published: 15 August 2026

common ferrite core, reached a peak efficiency above 90% and an approximately 50% wider spatial energy capture zone compared to standard horizontal DDQ layouts [8–10]. However, the number of vertical coils in that study was set to five based on initial design intuition rather than systematic optimization. As the number of vertically stacked coils increases, the effective magnetic flux capture area broadens and more energy is captured, yet the mutual inductance among the coils grows and can affect resonance characteristics and energy transfer stability [11]. Excessive coupling is known to disturb resonance frequency control and reduce overall efficiency [12]. Building upon the close agreement between simulation and experimental results established in our previous work [8], the present study focuses exclusively on a comprehensive, simulation-based investigation. The aim of this work is therefore to identify the optimal VC coil count for the given geometry.

Recent optimization work in DWPT often applies algorithmic parameter tuning, for example, multi-objective genetic algorithms, to maximize the coupling coefficient of planar magnetic structures [13,14]. These methods optimize sizing and spacing within a fixed topology rather than the topology itself. Multi-receiver WPT architectures are also well established, but they are generally designed to distribute power among separate independent loads [11,12], not to aggregate energy into a single high-power vehicle system. Planar layouts such as DDQ improve spatial coverage, yet their capture area is limited by a two-dimensional footprint [9]. Earlier work on the VC configuration showed its advantage over DDQ but used a fixed coil count [8]. Here, the coil count is swept from three to seven, which locates the threshold at which the wider magnetic capture area stops compensating for the growing mutual inductance between coils. The sweep also exposes a systematic difference between odd and even coil counts, which follows from whether a coil sits at the center of the ferrite core. This study differs from our previous work in aim and method. The prior study [8] was a proof of concept that established the VC advantage over the DDQ layout using a single five-coil receiver, validated experimentally, with the coil count fixed and its optimization left for later. Here, we take the VC as established and study the physics that sets its optimal design. We extract the full position-dependent coupling matrix $K(x)$ over the whole pass rather than at single points, and we report and explain an odd/even symmetry effect and the magnetization profile of the open ferrite core. To our knowledge, such a systematic sweep, combined with position-dependent coupling matrix extraction and an odd/even symmetry analysis, has not been reported for vertical receiver configurations.

2. Materials and Methods

To investigate how the number of receiving coils in the Vertical Coil (VC) configuration affects energy transfer efficiency, a quasi-static electromagnetic co-simulation framework was developed using COMSOL Multiphysics 6.2 [15] and LTspice 24.1.4 [16,17].

The accuracy of this combined COMSOL and LTspice simulation framework was previously established and experimentally validated in our foundational investigation of the Vertical Coil architecture [8]. Because the physical measurements of the baseline prototypes demonstrated high fidelity with the simulated outputs, the present study confidently leverages this computational approach to execute a high-resolution topological sweep, avoiding the prohibitive resource constraints of fabricating multiple distinct multi-coil arrays.

2.1. Electromagnetic Field Model and Coupling Extraction

In the COMSOL environment, the Magnetic Fields interface was used to solve Ampère's law across all domains. A spherical air domain bounded by a Magnetic Insulation boundary condition was established to represent the surrounding environment. The non-

https://doi.org/10.3390/en19163832

linear magnetic behavior of the ferrite core was captured using its measured B–H curve (Figure 1), taken from [18]. The material has an initial relative permeability of about 1600, rising to a peak of roughly 4200 near $H = 48$ A/m, and saturates toward $B \approx 0.68$ T at high field. Under the operating conditions of this study the core remains in the low-field, high-permeability region, well below saturation, so its response is effectively linear, as detailed in our previous work [8,19].

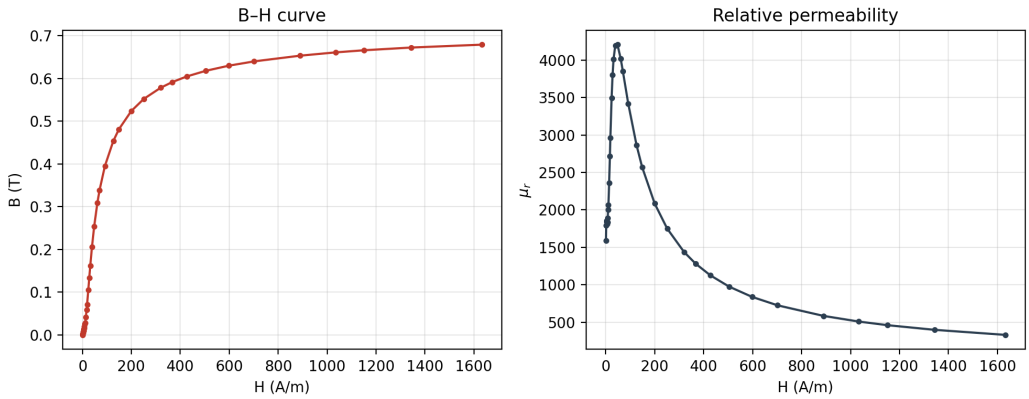

Figure 1. Measured B–H curve of the ferrite core (**left**) and the derived relative permeability μ_r versus field H (**right**) [18].

A mesh independence study was carried out before the whole simulation runs. The model was solved repeatedly with progressively refined free tetrahedral meshes, with additional refinement imposed in the ferrite domains and in the air gap between the transmitter and the receiver coils, where the field gradients are steepest. The extracted self and mutual inductances were monitored at each refinement level. Refinement was continued until successive levels changed these values by less than 1%, and the coarsest mesh satisfying this criterion was adopted for all simulations reported here. Further refinement beyond this point altered the extracted coupling coefficients only marginally while increasing the solution time substantially, confirming that the results are independent of the mesh resolution. The self-inductance of each coil was determined by applying a linear current ramp to the coil of interest while maintaining an open circuit across all other coils. Similarly, the mutual inductance for each coil pair was calculated by ramping the current in the primary coil and measuring the induced voltage across the secondary. The spatial mesh was generated using a Free Tetrahedral algorithm to ensure high-resolution capture of the local flux gradients. Through this method, the position-dependent coupling coefficients between the transmitting coil and each receiving coil were continuously extracted along the longitudinal axis of motion (x-axis), yielding the coupling matrix, $K(x)$.

2.2. Receiver Configurations and System Geometry

This study examined configurations consisting of three to seven vertically oriented receiver coils, each uniformly wound and symmetrically distributed along a common ferrite core. This range was selected to bracket the optimum symmetrically. Fewer than three coils cover too little of the core to form a useful high-efficiency zone, and the two-coil case leaves the core center unpopulated, giving low efficiency near alignment. Above seven coils, mutual coupling and detuning already dominate, and the declining trend seen for the six- and seven-coil arrays shows that adding further coils only reduces efficiency. Larger counts were therefore excluded as clearly past the optimum.

To strictly isolate the impact of the receiver coil count on system efficiency, the number of receiving coils was treated as the sole independent variable in this study. All other geometric, material, and electrical parameters were held strictly constant across all evaluated configurations (from three to seven coils) and are identical to the validated baseline established in [8]. For full reproducibility, the universal parameter settings applied to all configurations are detailed as follows: The transmitting coil comprises 11 turns, with outer dimensions of 50 cm by 50 cm, inner dimensions of 36.4 cm by 36.4 cm, and a thickness of 1 cm. The ferrite embedded within the transmitter measures 125 cm by 40 cm with a thickness of 6 cm. Regardless of the total number of coils in the array, every individual receiving coil consists of 10 turns, featuring outer dimensions of 10 cm by 50 cm, inner dimensions of 8 cm by 48 cm, and a height of 1 cm. The spacing between adjacent receiving coils remains constant in all arrays, and the vertical air gap distance from the receiver ferrite to the transmitting coils is fixed at 30 cm, as illustrated by the seven-coil configuration in Figure 2.

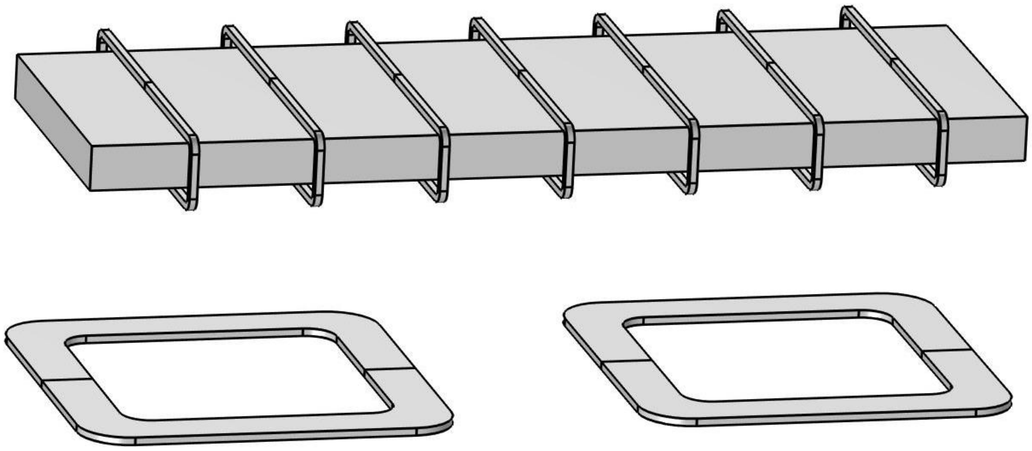

Figure 2. Geometric model of a representative VC receiver, shown here in its seven-coil configuration: vertically wound coils are symmetrically distributed along a common ferrite core, positioned above the transmitter coil array.

2.3. Circuit Co-Simulation

The calculated position-dependent coupling matrix, $K(x)$, was imported into LTspice to simulate the full RLC network for each longitudinal position x. The transmitting coil circuit was designed to resonate at 85 kHz, the standard frequency for EV DWPT systems. Each receiving coil was modeled as an independent resonant circuit with compensating [5,20] capacitances selected to achieve resonance at 85 kHz when perfectly aligned over the transmitter center, explicitly accounting for the mutual inductances derived from the FEA simulations [19,21]. The system uses an independent rectifier for each receiver coil before summing the DC power. This isolates the power contributions and prevents AC phase cancellation.

2.4. Efficiency and Harvested Energy Metrics

For each positional increment Δx along the driving lane, the circuit was solved in steady state. Let $V_s(x)$ and $I_s(x)$ represent the source voltage and current correspondingly, and let $I_{L,j}(x)$ and $V_{L,j}(x)$ be the current and voltage through the load resistor $R_{L,j}$ on receiver j, for $j = 1, \ldots, N_R$. The input power $P_{in}(x)$ and the discrete load power per coil $P_{out,j}(x)$ were calculated as:

$$P_{in}(x) = \frac{1}{T} \int_0^T V_s(t,x)\, I_s(t,x)\, dt \tag{1}$$

$$P_{out,j}(x) = \frac{1}{T} \int_0^T V_{L,j}(t,x)\, I_{L,j}(t,x)\, dt \tag{2}$$

https://doi.org/10.3390/en19163832

$$P_{out}(x) = \sum_{j=1}^{N_R} P_{out,j}(x) \tag{3}$$

The total output power and the instantaneous position-dependent efficiency $\eta_{total}(x)$ were then defined as:

$$\eta_{total}(x) = \frac{P_{out}(x)}{P_{in}(x)} \tag{4}$$

Finally, to quantify the total energy transferred during a complete pass over the transmitter, numerical integration was performed over the pass length $L_{pass} = 3$ m.

The integration length was set to 3 m (evaluated from -1.5 m to 1.5 m along the x-axis). As demonstrated by the spatial efficiency curves, (Figure 3 below) the magnetic field strength and resulting energy transfer efficiency decay to negligible values beyond this range. Because the harvested energy outside this 3 m span is effectively zero for all evaluated topologies, extending the integration bounds further does not yield any meaningful addition to the total energy and has no influence on the comparative ranking of the configurations.

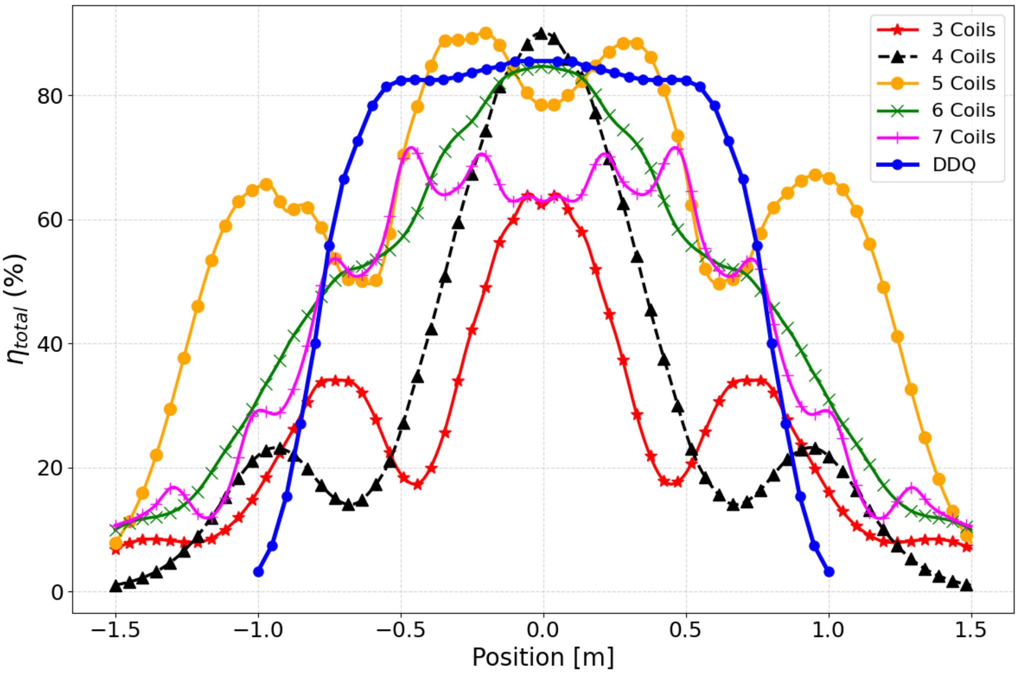

Figure 3. Position-dependent total efficiency, $\eta_{total}(x)$, for receiver configurations of three to seven vertical coils during a full pass over the transmitter, with the traditional horizontal DDQ receiver included as a benchmark (blue curve). Odd-numbered configurations exhibit a local minimum at $x = 0$, whereas the four-coil configuration attains the highest absolute peak. DDQ sustains a high, flat plateau near 85% but only within $|x| \lesssim 0.9$ m before dropping sharply, whereas the five-coil VC maintains efficiency over a wider span through its secondary peaks.

This integrated area, $A_{\eta,c}$, serves as a relative measure of the total harvested energy [22]. The input power is not constant along the pass: the source drives the transmitter tank at a fixed 85 kHz, so the delivered power follows the impedance reflected from the receiver array, which in turn depends on the position-dependent coupling $K(x)$. The compensation capacitances are matched at the aligned position, so the transmitter operates closest to its matched condition near $x = 0$ and is progressively detuned as the array moves away, where the weaker coupling lowers the reflected resistance seen by the source. This behaviour is inherent to the architecture and applies identically to every configuration, since all of them are driven by the same source under the same operating conditions. The metric is therefore used comparatively rather than as an absolute energy value, and the ranking it produces between configurations is unaffected. To compare configurations, this value was normalized against the maximum efficiency system:

$$A_{\eta,c} = \int_{-L_{pass}/2}^{L_{pass}/2} \eta_{total,c}(x)\, dx \tag{5}$$

$$A_{\eta,\text{norm}} = \frac{A_{\eta,c}}{\max(A_{\eta,c})} \times 100, \quad c = 3, \ldots, 7 \tag{6}$$

Here, c denotes the receiver configuration, that is, the number of coils in the array, and $\eta_{total,c}(x)$ is the total efficiency of configuration c, evaluated using Equation (4). The index c is used throughout for configurations and the index j for individual receiver coils within a configuration.

This procedure quantifies the dynamic efficiency trends and identifies the optimal coil array configuration.

The finite element extraction of $K(x)$ required approximately 90 s per position on average, depending on the number of receiver coils, which amounts to about 1.5 h for a full pass of 61 positions. This time is dominated by the ferrite domains, where the measured B–H curve is used instead of a constant permeability, so each position requires an iterative nonlinear solve rather than a single linear one. Note, however, that these estimations of computing time are hardware and software dependent and serve only as primary estimations.

The subsequent circuit solution in LTspice is negligible in comparison, since the coupling matrix enters as a precomputed input. Consequently, once $K(x)$ has been extracted for a given geometry, the compensation capacitances, loads, and operating point can be swept at almost no additional cost, which keeps the framework tractable over a broader design space.

3. Results and Discussion

3.1. Position-Dependent Efficiency of the Coil Arrays

First, position-dependent efficiency data were extracted from the COMSOL and LTspice co-simulations for each configuration of three to seven receiving coils. The calculated efficiencies were then combined into a single plot, illustrating the relationship between efficiency and receiver position along the x-axis, the direction of motion. Data points were sampled at 5 cm intervals, followed by numerical interpolation between these points. This high-resolution sampling ensures that all discernible features and fluctuations observed in the resulting curves accurately represent the simulated physical phenomena.

The spatial distribution of the total system efficiency, $\eta_{total}(x)$, as a function of the receiver position, shown in Figure 3, shows a complex dependence on the number of coils in the array. The behavior differs between configurations with an even and an odd number of coils:

- **Symmetry and central peaks:** Configurations with an odd number of coils (3, 5, and 7) exhibit a distinct local minimum at the central position ($x = 0$ cm). In contrast, even configurations, most notably the four-coil array, show a sharper, more concentrated central peak, whereas the six-coil configuration demonstrates a flatter distribution around the center, suggesting a more uniform efficiency zone at the cost of peak magnitude. This difference between odd and even configurations stems from the spatial distribution of the receivers relative to the magnetic flux profile at $x = 0$ alignment. Because the system employs independent rectifiers for each coil before summing the DC power, AC phase cancellation between coils is circumvented. Therefore, the variations in total efficiency are dominated by the magnitude of flux linkage and localized reactive detuning. In an odd-numbered configuration, a single receiver coil is positioned exactly at the geometric center of the ferrite core, where it experiences the absolute maximum B_x field. This intense local magnetization induces high currents in the central coil, which concurrently generates strong mutual coupling (M_{ij}) with its immediately adjacent flanking coils (the full coupling-coefficient matrices at this aligned position are provided in Appendix A). This localized cross-coupling detunes the adjacent resonant circuits precisely when the array is positioned at $x = 0$, resulting in a localized dip in the total efficiency. Conversely, an even-numbered configuration lacks a singular central coil. Instead, the array is symmetrically bifurcated. At $x = 0$, the two innermost coils straddle the central axis, allowing them to symmetrically capture the strong B_x field component. This yields the sharper, more concentrated total efficiency peak observed in the even-coil arrays.

- **Expansion of the high-efficiency zone:** As the number of coils increases, the "effective width" of the efficiency profile broadens. For the three-coil system, the efficiency drops rapidly beyond 50 cm, while the five- to seven-coil systems maintain non-negligible efficiency levels across a wider spatial range, albeit with stronger and more numerous oscillations.
- **Evolution of absolute maxima:** Increasing the number of coils does not monotonically increase the absolute peak efficiency. For instance, the four-coil configuration (dashed black curve) achieves the highest absolute efficiency, exceeding 90%, whereas further increasing the count to six or seven coils results in a reduction in the global maximum. This suggests an optimization limit where mutual coupling losses or impedance mismatches may begin to dominate.
- **Growth of secondary peaks:**Increasing the coil count also produces secondary and tertiary maxima. While the three-coil system shows only minor side lobes, the five- and seven-coil configurations exhibit pronounced secondary peaks (e.g., at approximately 100 cm for the five-coil case). These peaks indicate the regions where the receiver aligns with the staggered positions of the array, effectively extending the operational range of the system.
- **Comparison with the DDQ benchmark:** The horizontal DDQ receiver (blue) provides a high, flat efficiency plateau near 85% around the center, but its efficient zone is confined to $|x| \lesssim 0.9$ m and falls abruptly to zero beyond it. The five-coil VC configuration reaches a higher peak and, through its secondary lobes, sustains non-negligible efficiency over a markedly wider spatial range, consistent with the wider energy-capture zone reported in our previous work [8].

3.2. Core Magnetization and the Origin of the Efficiency Peaks

To understand the non-monotonic, multi-peaked shape of the efficiency curves in Figure 3, one must examine the magnetization state of the ferrite core during a full pass above the transmitter coils. Since the transmitter generates a bipolar spatial field-line distribution, the maximal B_x value is always obtained at $x = 0$. Therefore, each point inside the core experiences maximal local magnetization when it reaches the $x = 0$ position. However, as the core is magnetically open, demagnetization plays an important role, and the maximal magnetization varies along the core, peaking at its center. Figure 4 shows this behavior. The curve exhibits the maximal induced B_x value for each point when it reaches $x = 0$. For example, a point in the core positioned 0.4 m away from the core center would experience a maximal B_x value of 300 G when it reaches $x = 0$, while a point at the center would experience B_x of almost 500 G. At the very edge of the core (0.6 m from the center), maximal B_x would drop to 100 G. This implies that although each coil contributes the most to the harvested energy at $x = 0$, coils distanced from the center of the core contribute less than coils near the center due to their reduced induced flux and thus self-inductance. As a result, the position-dependent efficiency curve $\eta_{total}(x)$ is a superposition of all coils, each contributing a curve rising to its own maximal efficiency when it crosses $x = 0$ and falling thereafter, with its peak contribution dependent on the location of the coil on the core. This results in an increased number of peaks and dips with increasing number of vertical coils

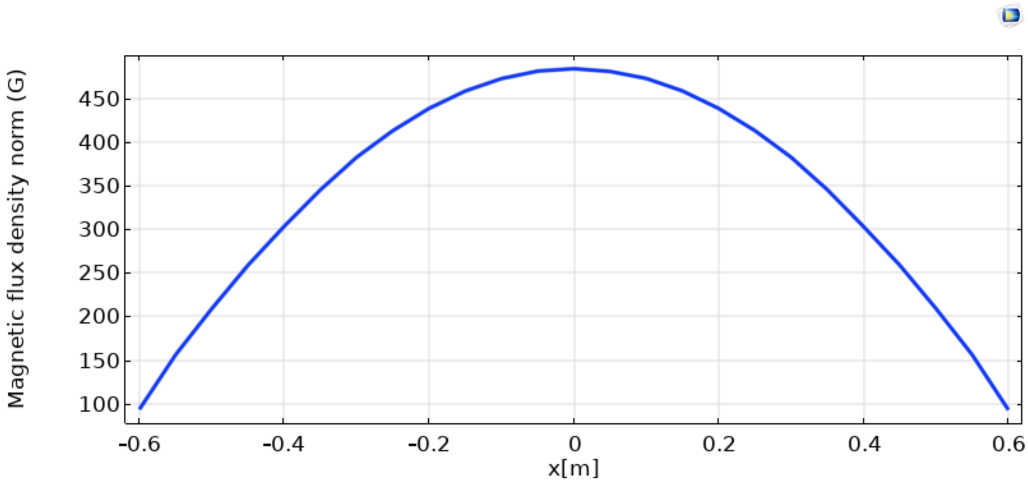

Figure 4. Maximal induced B_x experienced by each point along the ferrite core as that point crosses the transmitter center ($x = 0$), plotted versus the point's distance from the core center. Due to demagnetization in the open core, the peak field decreases from nearly 500 G at the core center to about 100 G at its edge (the vertical axis is given in gauss).

Figures 5–7 further elaborate on the main features of the position-dependent efficiency curves of Figure 3 for the simple three-coil VC case. Figure 5 exhibits the spatial distribution of B_x when the center coil is at $x = 0$. At this point, the central region of the core is magnetized over five times higher than its left and right regions. Therefore, the contribution of the center coil to the harvested energy is maximal while the other two coils contribute very little. When one of the other coils reaches $x = 0$ (Figure 6), its contribution peaks. However, this peak is lower than that of the center coil, as shown in Figure 4. Figure 7 displays an interesting position at $x = 0.75$ m, where the center coil is no longer above the transmitter. Yet, the VC configuration enables it to pick up the flux returning to the transmitting coils in reversed polarity and still generate a positive contribution to the harvested energy. Summing it all, a full pass above the transmitter results in the red curve of Figure 3, which is the superposition of the contributions of all local maxima and minima of each coil. With increasing number of coils, the number of such local maxima and minima increases, the position-dependent efficiency exhibits high-frequency spatial oscillations, and its middle section (around $x = 0$) flattens.

3.3. Total Harvested Energy Versus Coil Count

Figure 3 presents the position-dependent efficiency for the various VC configurations. Clearly, the area beneath each curve, which represents the total energy picked up by the receiver in a full pass, varies with the number of coils. Figure 8 presents this area, normalized according to Equation (6), $A_{\eta,\text{norm}}$, versus the number of coils. The five-coil configuration yields the highest harvested energy. Initially, adding more spaced-apart coils increases the total flux picked up by the receiver. Beyond five coils, however, the mutual induction within the system increases. The heightened mutual induction induces detrimental cross-coupling, making resonance conditions harder to achieve and maintain, thereby reducing the overall efficiency of the coils in absorbing and delivering energy.

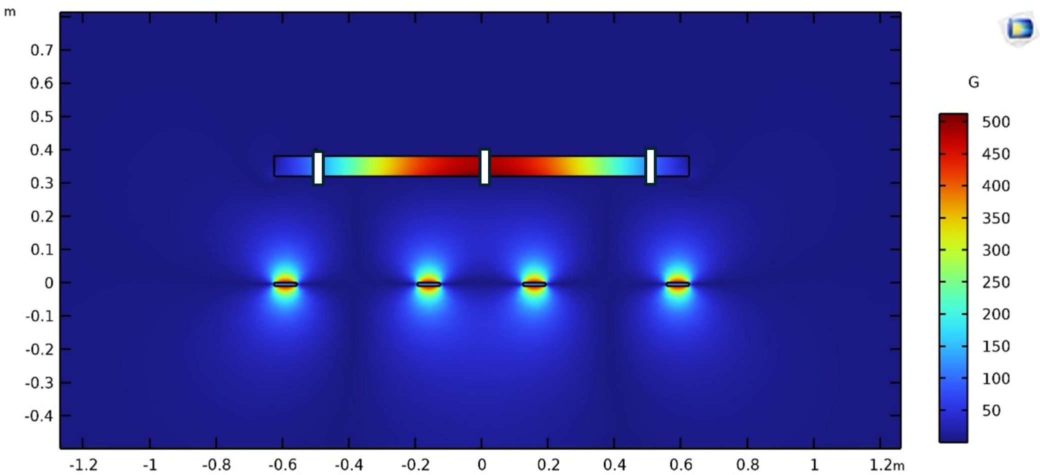

Figure 5. $|B_x|$ field distribution in the XZ plane for the three-coil VC configuration, with the receiver centered above the transmitter ($x = 0$ cm). The flux concentrates in the central region of the core, so the central coil dominates the harvested energy at this position.

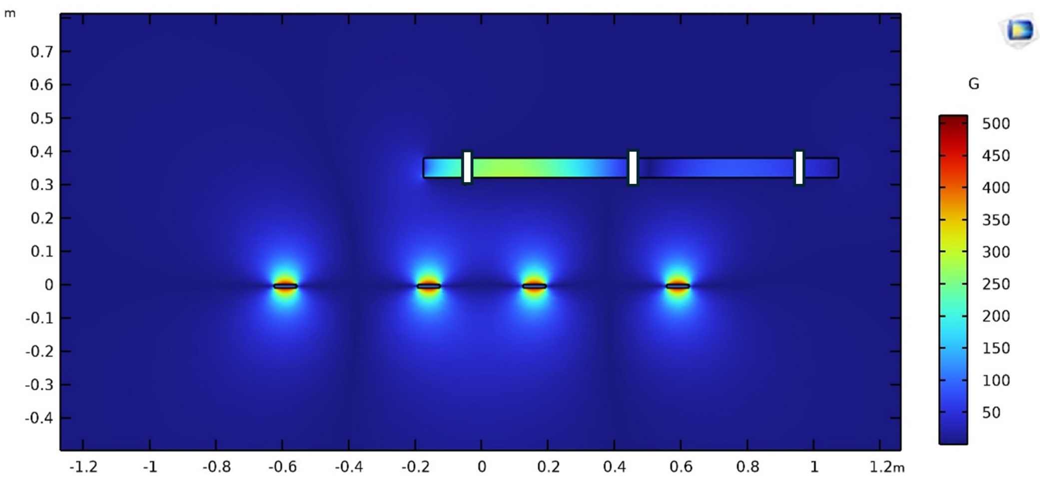

Figure 6. $|B_x|$ field distribution in the XZ plane at $x = 45$ cm, where a side coil is aligned with the transmitter center. Its contribution peaks at this position, but remains lower than that of the central coil (cf. Figure 4).

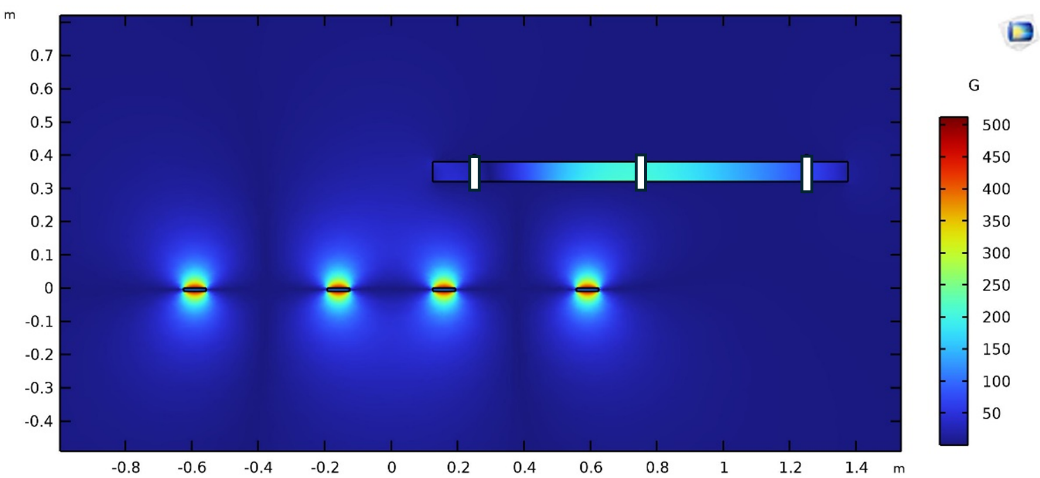

Figure 7. $|B_x|$ field distribution in the XZ plane at $x = 75$ cm. Although the central coil is no longer above the transmitter, it captures the return flux in reversed polarity and still contributes positively to the harvested energy.

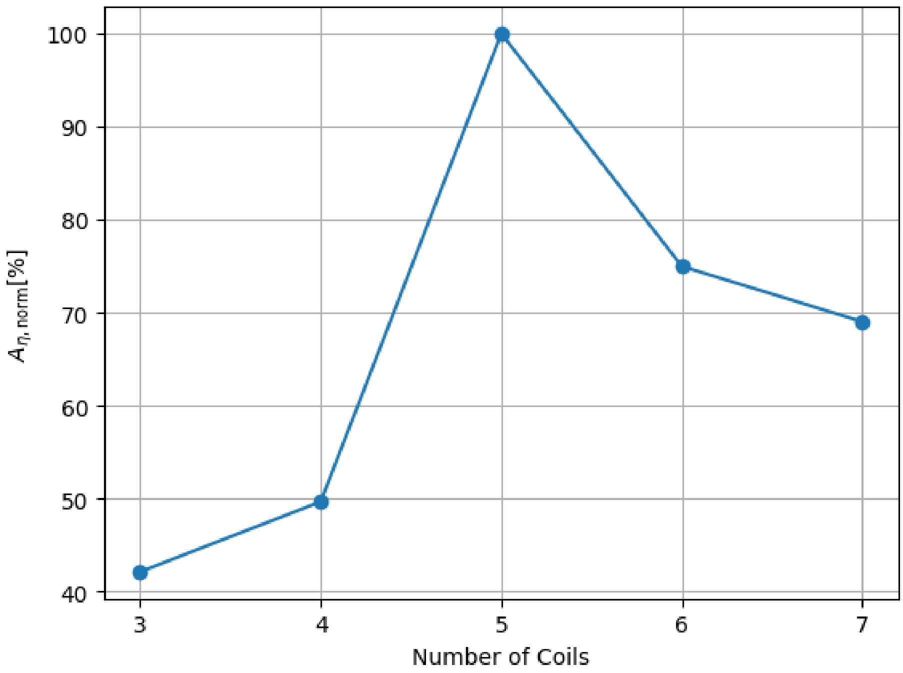

Figure 8. Normalized harvested energy, $A_{\eta,\mathrm{norm}}$ (Equation (6)), as a function of the number of receiver coils. The five-coil configuration maximizes the total energy harvested per pass. adding a sixth or seventh coil reduces it due to detrimental cross-coupling.

3.4. Cross-Coupling and Resonance Detuning

The addition of further coils beyond five introduces detrimental cross-coupling that degrades system performance. In a multi-coil array, the equivalent inductance of any individual receiver coil i is modified by the magnetic field induced in adjacent coils j. The effective inductance can be expressed as:

$$L_{eff,i} = L_i + \sum_{j \neq i} M_{ij} \left(\frac{I_j}{I_i} \right) \tag{7}$$

where L_i is the self-inductance and M_{ij} is the mutual inductance between the coils. Because the resonant compensation network uses fixed capacitors (C_i) tuned specifically to the isolated self-inductance $\left(C_i = 1/(\omega^2 L_i)\right)$, the heightened mutual induction in densely packed arrays shifts the effective inductance. This shift detunes the receiver circuits away from the target 85 kHz operating frequency. The reactive impedance then increases, resonance becomes harder to maintain, and the coils absorb and deliver less real power to the load.

4. Conclusions

This work systematically investigated the effect of vertical receiver coil quantity on the total harvested energy in DWPT systems. By combining position-dependentr efficiency curves with magnetic field inspection ($|B_x|$ maps) at representative spatial intervals, we obtained a physical interpretation of the performance trends.

The key findings of this article are:

- The relationship between coil count and transferred energy is non-monotonic.
- For the specified geometry and spacing, the normalized harvested energy reaches an optimal peak at five vertical coils.
- The addition of a sixth or seventh coil introduces detrimental cross-coupling that detunes the receivers and reduces the total harvested energy.

This optimum is explained through the interplay of local field concentration and demagnetization effects within the open ferrite core. Magnetic field analysis shows that at the central alignment ($x = 0$), flux concentrates is higher in the mid-section of the core, maximizing the contribution of the central coil while the outer coils experience a substantially weaker field. As the receiver array moves along the transmission path, the field redistributes. Consequently, the position-dependent efficiency exhibits high-frequency spatial oscillations driven by the localized maxima and minima of individual coils. An evaluation of the horizontal field component distribution (B_x vs. x) provides a direct link between the local field strength at each coil and its discrete contribution to the total harvested energy. With these geometric guidelines and further validation, the VC architecture is a promising DWPT receiver. Quantification of system-level impacts on battery sizing and driving range requires further experimental and system-level studies.

It is important to note that the five-coil optimum identified in this study is specific to the evaluated baseline geometry and fixed spatial parameters. The primary focus of this work was to isolate and demonstrate the fundamental non-monotonic trade-off between expanding the flux capture area and the corresponding escalation of mutual inductance. Because electromagnetic coupling is highly sensitive to physical boundary conditions, altering parameters such as the vehicle air gap, inter-coil spacing, or core dimensions could shift the optimal coil count. Having established this baseline topological behavior, ongoing and future studies will engage in comprehensive sensitivity analyses. These subsequent investigations will explore variable coil spacing, asymmetric winding configurations, dynamic air gaps, and alternative core materials to fully map the multi-parameter optimization space required for commercial DWPT deployment.

The present model assumes ideal coil alignment along the longitudinal axis. lateral misalignment, yaw, and pitch offsets are not considered. Thermal effects, conductor resistivity variation with temperature, and electromagnetic interference from the vehicle chassis are not included. Ferrite material properties are modeled using a static B–H curve. These simplifications are appropriate for establishing first-order design guidelines but should be revisited in future work incorporating 3D misalignment sweeps and experimental thermal measurements.

Author Contributions: Conceptualization, I.G. (equal) and S.W. (equal). Data Curation, I.G. (lead). Formal Analysis, I.G. (lead). Funding Acquisition, S.W. (lead). Investigation, I.G. (lead) and S.W. (equal). Methodology, I.G. (lead) and Y.N. (supporting). Project Administration, S.W. (lead). Resources, S.W. (lead). Supervision, S.W. (lead). Validation, S.W. (lead). Visualization, I.G. (lead). Writing original draft, I.G. (lead). Writing review & editing, Y.N. (supporting) and S.W. (supporting). All authors have read and agreed to the published version of the manuscript.

Funding: The research presented in this paper was (partially) funded by the Israeli Smart Transportation Research Center (ISTRC).

Institutional Review Board Statement: Not applicable.

Informed Consent Statement: Not applicable.

Data Availability Statement: The data that support the findings of this study are available upon reasonable request from the authors. The data are not publicly available due to intellectual property constraints and their direct relevance to ongoing, unpublished research.

Conflicts of Interest: Author Yasha Nikulshin was employed by the company N.T. TAO Ltd. The remaining authors declare that the research was conducted in the absence of any commercial or financial relationships that could be construed as a potential conflict of interest

Abbreviations and Nomenclature

The following abbreviations are used in this manuscript:

DWPT	Dynamic Wireless Power Transfer
EV	Electric Vehicle
WPT	Wireless Power Transfer
VC	Vertical Coil
DDQ	Double-D Quadrature (coil topology)
FEA	Finite Element Analysis
RLC	Resistor–Inductor–Capacitor

The following symbols are used in this manuscript:

Symbol	**Description**	**Unit**
Geometry and position		
x	Longitudinal position of the receiver along the direction of motion	m
Δx	Positional increment between successive simulation steps	m
L_{pass}	Length of a full pass over the transmitter	m
N_R	Number of receiver coils in the array	–
i, j	Receiver coil indices within a configuration	–
c	Receiver configuration index, equal to the number of coils in the array	–
Circuit quantities		
$K(x)$	Position-dependent coupling matrix between transmitter and receiver coils	–
L_i	Self-inductance of receiver coil i	H
M_{ij}	Mutual inductance between coils i and j	H
$L_{eff,i}$	Effective inductance of coil i including mutual contributions	H
C_i	Compensation capacitance of receiver circuit i	F
$R_{L,j}$	Load resistance connected to receiver j	Ω
V_s, I_s	Source voltage and source current	V, A
$V_{L,j}$, $I_{L,j}$	Voltage across and current through the load of receiver j	V, A
ω	Angular resonant frequency	rad/s
t, T	Time and period of the steady-state waveform	s
Power and efficiency		
P_{in}	Input power delivered by the source	W
$P_{out,j}$	Output power dissipated in the load of receiver j	W
P_{out}	Total output power summed over all receivers	W
$\eta_{total}(x)$	Position-dependent total efficiency of the receiver array	%
$\eta_{total,c}(x)$	Total efficiency of configuration c	%
$A_{\eta,c}$	Integrated efficiency of configuration c over a full pass	%·m
$A_{\eta,\text{norm}}$	Harvested energy normalized to the best configuration	%
Symbol	**Description**	**Unit**
Magnetic quantities		
B	Magnetic flux density	T
B_x	Longitudinal component of the magnetic flux density	T
H	Magnetic field strength	A/m
μ_r	Relative permeability of the ferrite core	–

Appendix A. Coupling-Coefficient Matrices at the Aligned Position

This appendix reports the coupling-coefficient matrices $k_{ij} = M_{ij}/\sqrt{L_i L_j}$ of the VC receiver at the aligned position ($x = 0$) for every evaluated configuration (three to seven coils). Each matrix is symmetric with a unit diagonal. the highest-numbered coil is the transmitter (ground) coil and the remaining coils form the receiver array. The aligned position represents the strongest-coupling condition and corresponds to the central resonance detuning discussed in the result Section. The nearest-neighbour receiver coupling grows monotonically with coil count, from $k \approx 0.25$ (three coils) to $k \approx 0.48$ (five coils) and $k \approx 0.56$ (six and seven coils), quantifying the increase in M_{ij} that drives the efficiency reduction seen in Figure 3.

Table A1. Coupling-coefficient matrix $k_{ij} = M_{ij}/\sqrt{L_i L_j}$ of the 3-coil VC receiver model at the aligned position ($x = 0$). L_6 is the transmitter (ground) coil. L_1, L_3, L_5 form the 3-coil receiver array.

	L_1	L_2	L_3	$L_{transmitting}$
L_1	1	0.2546	0.0983	0.0298
L_2	0.2546	1	0.2544	0.1051
L_3	0.0983	0.2544	1	0.0298
$L_{transmitting}$	0.0298	0.1051	0.0298	1

Dimensionless. symmetric with unit diagonal.

Table A2. Coupling-coefficient matrix $k_{ij} = M_{ij}/\sqrt{L_i L_j}$ of the 4-coil VC receiver model at the aligned position ($x = 0$). L_6 is the transmitter (ground) coil. L_1–L_4 form the 4-coil receiver array.

	L_1	L_2	L_3	L_4	$L_{transmitting}$
L_1	1	0.4544	0.3034	0.1970	0.0595
L_2	0.4544	1	0.4870	0.3034	0.0998
L_3	0.3034	0.4870	1	0.4546	0.0998
L_4	0.1970	0.3034	0.4546	1	0.0595
$L_{transmitting}$	0.0595	0.0998	0.0998	0.0595	1

Dimensionless. symmetric with unit diagonal.

Table A3. Coupling-coefficient matrix $k_{ij} = M_{ij}/\sqrt{L_i L_j}$ of the 5-coil VC receiver model at the aligned position ($x = 0$). L_6 is the transmitter (ground) coil. L_1–L_5 form the 5-coil receiver array.

	L_1	L_2	L_3	L_4	L_5	$L_{transmitting}$
L_1	1	0.393	0.258	0.174	0.100	0.030
L_2	0.393	1	0.477	0.309	0.174	0.083
L_3	0.258	0.477	1	0.477	0.258	0.105
L_4	0.174	0.309	0.477	1	0.392	0.083
L_5	0.100	0.174	0.258	0.392	1	0.030
$L_{transmitting}$	0.030	0.083	0.105	0.083	0.030	1

Dimensionless. symmetric with unit diagonal.

Table A4. Coupling-coefficient matrix $k_{ij} = M_{ij}/\sqrt{L_i L_j}$ of the 6-coil VC receiver model at the aligned position ($x = 0$). L_7 is the transmitter (ground) coil. L_1–L_6 form the 6-coil receiver array.

	L_1	L_2	L_3	L_4	L_5	L_6	$L_{transmitting}$
L_1	1	0.5007	0.3632	0.2771	0.2099	0.1487	0.0457
L_2	0.5007	1	0.5492	0.4017	0.2992	0.2099	0.0814
L_3	0.3632	0.5492	1	0.5621	0.4019	0.2772	0.1025
L_4	0.2771	0.4017	0.5621	1	0.5493	0.3634	0.1025
L_5	0.2099	0.2992	0.4019	0.5493	1	0.5010	0.0814
L_6	0.1487	0.2099	0.2772	0.3634	0.5010	1	0.0457
$L_{transmitting}$	0.0457	0.0814	0.1025	0.1025	0.0814	0.0457	1

Dimensionless. symmetric with unit diagonal.

Table A5. Coupling-coefficient matrix $k_{ij} = M_{ij}/\sqrt{L_i L_j}$ of the 7-coil VC receiver model at the aligned position ($x = 0$). L_8 is the transmitter (ground) coil. L_1–L_7 form the 7-coil receiver array.

	L_1	L_2	L_3	L_4	L_5	L_6	L_7	$L_{transmitting}$
L_1	1	0.4613	0.3308	0.2539	0.1965	0.1472	0.0978	0.0300
L_2	0.4613	1	0.5368	0.3944	0.3000	0.2226	0.1470	0.0665
L_3	0.3308	0.5368	1	0.5634	0.4113	0.3000	0.1962	0.0959
L_4	0.2539	0.3944	0.5634	1	0.5635	0.3946	0.2537	0.1062
L_5	0.1965	0.3000	0.4113	0.5635	1	0.5371	0.3308	0.0959
L_6	0.1472	0.2226	0.3000	0.3946	0.5371	1	0.4613	0.0665
L_7	0.0978	0.1470	0.1962	0.2537	0.3308	0.4613	1	0.0300
$L_{transmitting}$	0.0300	0.0665	0.0959	0.1062	0.0959	0.0665	0.0300	1

Dimensionless. symmetric with unit diagonal.

References

1. Kurs, A.; Karalis, A.; Moffatt, R.; Joannopoulos, J.D.; Fisher, P.; Soljačić, M. Wireless Power Transfer via Strongly Coupled Magnetic Resonances. *Science* **2007**, *317*, 83–86. https://doi.org/10.1126/science.1143254.
2. Panchal, C.; Stegen, S.; Lu, J. Review of static and dynamic wireless electric vehicle charging system. *Eng. Sci. Technol. Int. J.* **2018**, *21*, 922–937. https://doi.org/10.1016/j.jestch.2018.06.015.
3. Herceg, D.; Rajs, V.; Živadin Despotović.; Popadić, B.; Šiljegović, M.; Kiraly, Z.; Vizvari, Z.; Wizner, K.; Felde, I.; Odry, P.; et al. Double-Layer Coils Design for 11 kW Wireless Power Transfer. *Electronics* **2024**, *13*, 547. https://doi.org/10.3390/electronics13030547.
4. Wang, X.; Pang, J.; Zhao, N.; Liu, L.; Dong, H.; Tan, Q.; Xiong, J. Lateral and angular misalignments of coil in wireless power transfer system. *Sens. Actuators A Phys.* **2022**, *341*, 113577. https://doi.org/10.1016/j.sna.2022.113577.
5. Covic, G.A.; Boys, J.T. Inductive Power Transfer. *Proc. IEEE* **2013**, *101*, 1276–1289. https://doi.org/10.1109/JPROC.2013.2244536.
6. Pashaei, A.; Aydin, E.; Ozdemir, M.A.; Kosesoy, Y.; Aydemir, M.T. A novel hybrid coil design and implementation for wireless power transfer systems. *Sci. Technol. Energy Transit.* **2024**, *79*, 74. https://doi.org/10.2516/stet/2024082.
7. Pahlavan, S.; Shooshtari, M.; Jafarabadi Ashtiani, S. Star-Shaped Coils in the Transmitter Array for Receiver Rotation Tolerance in Free-Moving Wireless Power Transfer Applications. *Energies* **2022**, *15*, 8643. https://doi.org/10.3390/en15228643.
8. Garrofy, I.; Roitman, A.; Nikulshin, Y.; Wolfus, S. Vertical Receiver Coils for Improved Energy Transfer Efficiency in Dynamic Wireless Charging of Electric Vehicles. *Appl. Sci.* **2025**, *15*, 3706. https://doi.org/10.3390/app15073706.
9. Domajnko, J.; Prosen, N. A Wireless Power Transfer System Using a Double DD Quadrature Coil Structure. *Electronics* **2023**, *12*, 890. https://doi.org/10.3390/electronics12040890.
10. Sahar, B. Effect of Coil Configuration on Dynamic Wireless Power Transfer for Electric Vehicle Applications, 2021. Available online: https://superconductivity.biu.ac.il/sites/superconductivity/files/shared/asap030118effectofcoilsgeometryondynamicwirelesspowertransferforelectricvehicles.pdf (accessed on 5 June 2026).
11. Xun, J.H.; Mu, Y.; Zhang, K.; Liu, H.; Li, L. The Efficiency Improvement of Multiple Receivers in Wireless Power Transmission by Integrating Metasurfaces. *Materials* **2022**, *15*, 6943. https://doi.org/10.3390/ma15196943.
12. Luo, Y.; Dai, Z.; Yang, Y. A Single-Transmitter Multi-Receiver Wireless Power Transfer System with High Coil Misalignment Tolerance and Variable Power Allocation Ratios. *Electronics* **2024**, *13*, 3838. https://doi.org/10.3390/electronics13193838.
13. Tang, W.; Jing, L.; Cao, W.; Xu, W.; Wu, X.; Liao, H. Optimization of magnetic coupling mechanism of dynamic wireless power transfer based on NSGA-II algorithm. *Sci. Rep.* **2024**, *14*, 5121. https://doi.org/10.1038/s41598-024-55512-9.
14. Zhang, H.; Sui, X.; Sui, P.; Wei, L.; Huang, Y.; Yang, Z.; Yang, H. Coil Parameter Optimization Method for Wireless Power Transfer System Based on Crowding Distance Division and Adaptive Genetic Operators. *Energies* **2024**, *17*, 3289. https://doi.org/10.3390/en17133289.
15. COMSOL. *COMSOL Multiphysics®*, v. 6.4; COMSOL AB: Stockholm, Sweden, 2026. Available online: https://www.comsol.com (accessed on 5 June 2026).
16. Analog Devices, Inc.. *LTspice®*, (Version 24.1.4); Analog Devices: Wilmington, MA, USA, 2024. Available online: https://www.analog.com/en/design-center/design-tools-and-calculators/ltspice-simulator.html (accessed on 5 June 2026).
17. Gabino, A. LTspice: Simple Steps for Simulating Transformers. 2014. Available online: https://www.analog.com/en/resources/technical-articles/ltspice-basic-steps-for-simulating-transformers.html (accessed on 13 January 2026).
18. Laird Technologies. MP Series Ferrite Plate MP3940-0M0 — Material Parameters. Available online: https://www.laird.com/products/inductive-components-emc-components-and-ferrite-cores/ferrite-plates-and-disks/mp-series/mp3940-0m0 (accessed on 5 June 2026).

19. Linden, J.; Nikulshin, Y.; Wolfus, S.; Rumbak, H.; Ezer, O.; Yeshurun, Y. Method for calculating coupling coefficients in dynamic energy transfer for electric vehicles. In *2017 Electric Vehicles International Conference (EV)* ; IEEE: Piscataway, NJ, USA , 2017; Volume 10 ; pp. 1–4. https://doi.org/10.1109/EV.2017.8242111.
20. Jiang, C.; Chau, K.T.; Liu, C.; Lee, C.H.T. An Overview of Resonant Circuits for Wireless Power Transfer. *Energies* **2017**, *10*, 894. https://doi.org/10.3390/en10070894.
21. Schormans, M.; Valente, V.; Demosthenous, A. Frequency Splitting Analysis and Compensation Method for Inductive Wireless Powering of Implantable Biosensors. *Sensors* **2016**, *16*, 1229. https://doi.org/10.3390/s16081229.
22. Moncada, O.; Imran, Z.; Vickers, C.; Gkritza, K.; Pekarek, S.; Aliprantis, D.; Brovont, A.; Jahangiri, B.; Haddock, J.E. *Full-Scale Dynamic Wireless Power Transfer and Pilot Project Implementation*; Technical Report; Joint Transportation Research Program: West Lafayette, IN, USA , 2024. https://doi.org/10.5703/1288284317744.